Journal of *Marine Science and Engineering*

MDPI

Article

A Semi-Analytical Method for the Sealing Performance Prediction of Subsea Pipeline Compression Connector

Zhenyu Li [1], Gang Wang [2,*], Shaoming Yao [1], Feihong Yun [1], Peng Jia [1], Chao Li [1] and Liquan Wang [1]

[1] College of Mechanical and Electrical Engineering, Harbin Engineering University, Harbin 150001, China; jade10623@sina.com (Z.L.); yao.sm@hotmail.com (S.Y.); yunfeihong@hrbeu.edu.cn (F.Y.); 13633605161@139.com (P.J.); 54529880@hrbeu.edu.cn (C.L.); wangliquan@hrbeu.edu.cn (L.W.)
[2] College of Shipbuilding Engineering, Harbin Engineering University, Harbin 150001, China
* Correspondence: wanggang@hrbeu.edu.cn

Abstract: To predict the sealing performance of the subsea pipeline compression connector, a semi-analytical method is proposed and verified. The leakage condition is obtained as a function of the minimum radial deflection. The semi-analytical method consists of three parts: a macroscopic analytical model for the interference process deduced based on the membrane theory, a mesoscopic two-dimensional finite element analysis of the internally turned sealing surface according to scanning electron microscope observation, and a formulation of the leakage ratio according to the Abbott–Firestone curve. The influences of the geometry parameters are analyzed. The prediction and identification of the leakage condition near the minimum preloaded deflection are investigated. Experimental tests are also carried out to verify the proposed method. The results show that, within five times the pipeline threshold of the thin wall thickness, compression connectors designed by the proposed method can create a reliable seal with a rough internally turned surface, saving 57% of the design time while reducing the machining time and costs.

Keywords: semi-analytical method; leakage ratio; compression connector; metal static seal; membrane theory; Abbott–Firestone curve

Citation: Li, Z.; Wang, G.; Yao, S.; Yun, F.; Jia, P.; Li, C.; Wang, L. A Semi-Analytical Method for the Sealing Performance Prediction of Subsea Pipeline Compression Connector. *J. Mar. Sci. Eng.* **2023**, *11*, 854. https://doi.org/10.3390/jmse11040854

Academic Editor: Bruno Brunone

Received: 20 March 2023
Revised: 13 April 2023
Accepted: 17 April 2023
Published: 18 April 2023

1. Introduction

Non-welded connections are increasingly used for the maintenance of subsea pipelines in marine industries [1]. The compression connector is one of the most efficient connectors that belongs to the mechanically attached connection (ASTM F1387 [2], ISO 8434-1 [3]). This technology has been developed by many well-known companies, including the Phastite® connector from PARKER HANNIFIN, the Tube-Mac® connector from PYPLOK® Corp., the compression connector from HAELOK®, etc. The connector is directly attached to the pipe by the mechanical deformation and creates a seal and a permanent joint by elastic–plastic deformation. The sealing principle is a metal static seal that uses the plastic deformation of the metal to block the leakage channel.

In studies on the leak ratio on randomly rough surfaces, the topography formed by the turning texture shows unique sealing properties [4]. This can be traced back to groundbreaking studies on the surface waviness theory [5] and further developments on surface roughness [6] and sealing design factors [7]. In the aspect of the gasket, Nakamura and Funabashi [8] observed the leakage on a spiral-like topography. Then, by establishing a simplified semi-empirical leakage model, Polycarpou and Etsion [9] demonstrated the importance of micro-profile parameters for the sealing performance of the metal gasket seal. To further understand the sealing performance of the turning topography, Geoffroy and Prat [10] established the seal leakage model of the face-turned metal gasket and found the transition from the radial leakage to the spiral leakage by studying the radial and circumferential leakage paths. Liao et al. [11] first presented the simplification of the radial

leakage path and the radial leakage model to clarify the effects of the micro-profile parameters on the sealing behaviors. More recently, the influence of wavy deformations and the formation of synthetic "turned-like" surfaces have been extensively studied. Scholars have also conducted much research on sealing topography related to the studies of asperity [12] and the probabilistic models [13] of rough surfaces. By establishing a 2D stochastic model, Marie et al. [14] developed a practical model and applied the multiscale calculation method based on the leakage ratio of the sealing structure. Liao et al. [15] proposed a method to decompose 3D surfaces into multi-scale surfaces by using wavelets to predict surface functions and detect machining errors. Deltombe et al. [16] used multi-scale analysis to characterize sealing performance. By comparing the differences between machining and superfinishing, it was shown that micro-roughness plays a major role in the leakage. In addition, Bricaud et al. [17] studied the leakage between firmly pressed rigid surfaces by measuring mass flow under different contact geometries using leakage tests.

Scholars have also conducted much research on compression connections. Weddeling et al. [18] derived an analytical model to determine the charging energy to a clamped connection with a mandrel inside the pipe. In another study, Weddeling et al. [19] developed a formula for the transferable load of connection with different groove shapes using membrane theory. Wei et al. [20] deduced the formula of the sealing pressure of a compression connector based on the superposition theorem of elasticity, and obtained the sealing condition using the finite element method (FE). Henriksen et al. [21] used experimental data and FE simulations to describe and understand the forces and deformations during the connection process and identified the increase radial stiffness as the best indicator of a clamped pipe flange connection while also predicting the load capacity of the connection. Wang et al. [22] proposed an optimization method for a compression connector based on a static metal sealing mechanism and optimized the structure using an FE model with the zero-order method. Onyegiri et al. [23] investigated a compression connector used on sandwich pipes combining 2D axisymmetric and 3D FE models. Quispe et al. [24] proposed a 2D FE model for threaded compression connection with square teeth and a metal static seal to join subsea sandwich pipes. Yan and Fan [25] employed a multiscale model to study the effect of the fluid pressure on the sealing performance of a pipeline connection. Agrawal et al. [26] developed a new method for a compression connector and carried out the extrusion test and compression test, concluding that the connection strength is considerable with welding. Liu et al. [27] optimized the anchoring structure by using a nonlinear FE analysis method. Wu et al. [28] introduced an axial load-bearing capacity calculation method for steel pipe-to-sleeve grouted connections, which also showed the significance of the compression connection.

For the compression connection, there is no simple analytical method to determine the achievable joint strength based on the process and joint characteristics [19,29]. In practice, the FE method is still the only option in many cases, resulting in a long design cycle and high test costs. Better knowledge and understanding of the elasticity and plastic deformation of the compression connection is required. In addition, most of the research on metal seals are about face-turned seals. Few studies can be found on the internally turned seal. The purpose of this study is to propose an effective semi-analytical method to predict the leakage ratio on the internally turned sealing surface of the compression connector, and, by analyzing the sealing behavior on the mesoscopic scale, to predict the leakage ratio for all standard pipe series.

The paper is organized as follows: In Section 2, the structure and fitting process of the compression connector are explained. In Section 3, an analytical model of the radial interference process is derived based on the membrane theory and verified by a macroscopic FE model. In Section 4, the SEM observation of the internally turned sealing surface is performed, and a mesoscopic FE model for the seal is developed. Then, the change law of the sealing surface during the compression is analyzed. In Section 5, by transferring the

deflection into the mesoscopic FE model, and using the Abbott–Firestone curve, the leakage ratio formulation is derived. In Section 6, a parameter analysis and experimental tests are presented.

2. Connector Fitting Process

The pipeline compression connector, the fitting tools, and the fitting process are shown in Figure 1. The connector is designed to maintain and/or repair typical single-wall subsea pipes with a diameter between 2 and 12 inches.

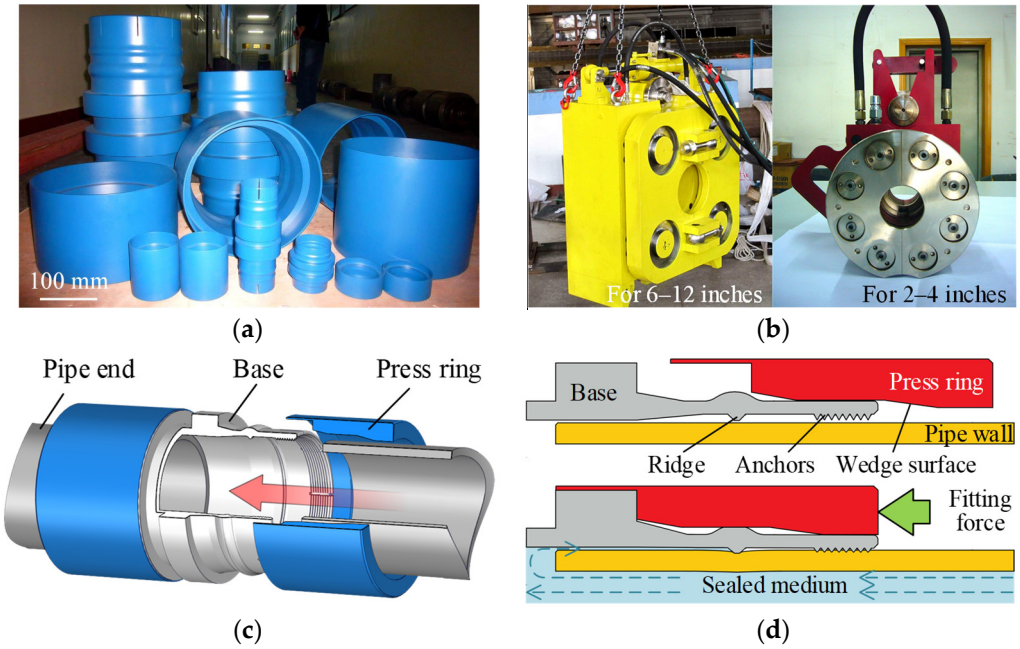

Figure 1. (**a**) Compression connector parts; (**b**) fitting tools; (**c**) connector assembly; (**d**) fitting process.

As shown in Figure 1, the connector consists of a base and a pair of press rings, which are made of metal and are symmetrically arranged along the pipe. Inside the base, there are one or more ring-shaped ridges for sealing and anchors (optional configuration) for gripping. A hydraulic fitting tool is used to drive the press rings to create a static compression metal seal [30]

3. Analytical Model of the Fitting Process

During the fitting process, external loads are transferred through the press ring, the shaped ridges are compressed on the sealing surface of the pipe and partially press into the pipe surface, creating a form-fit [31] sealing condition. The geometries can be idealized as 2D axisymmetric thin-walled cylinders [32] and the membrane theory of symmetrically loaded cylinders based on Kirchhoff's hypothesis [33] is applicable. The internal forces can be solved by the physical relations between stress and strain, the differential equations of the deflections, and the relations between strain and displacement.

3.1. Formulation

A shell element of the thin-walled long cylinder with mid-surface radius R and thickness δ is shown in Figure 2. The mid-surface of the shell is located at the cylindrical coordinates system with angle φ, axial position x, and radius $\rho(=R+z)$. The corresponding displacements on the mid-surface are $u, v,$ and w. P_x is the shearing force, N_φ and N_x are the membrane forces, and M_φ and M_x are the bending moments. N_φ and M_φ are constant in the circumference.

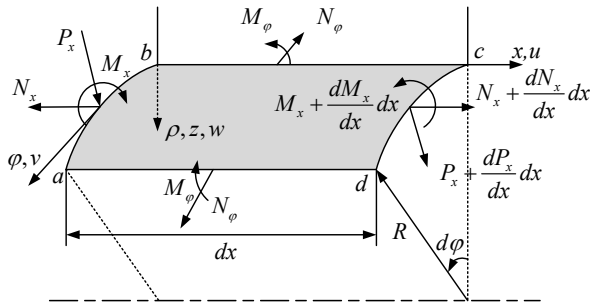

Figure 2. A thin-walled cylindrical shell in the cylindrical coordinates.

Assuming that external forces only contribute to the normal pressure on the surface, the following geometrical and equilibrium equations apply:

$$\frac{dN_x}{dx} = 0, \qquad \frac{dP_x}{dx} + \frac{N_\varphi}{R} + P_z = 0, \qquad \frac{dM_x}{dx} - P_x = 0 \tag{1}$$

The expressions for the strains can be written as

$$\varepsilon_x = \frac{du}{dx}, \varepsilon_\varphi = -\frac{w}{R}, \tag{2}$$

and, when applying Hook's law and yield,

$$\begin{cases} N_x = \dfrac{E\delta}{1-\upsilon^2}\left(\varepsilon_x + \nu\varepsilon_\varphi\right) = \dfrac{E\delta}{1-\upsilon^2}\left(\dfrac{du}{dx} - \nu\dfrac{w}{R}\right) \\ N_\varphi = \dfrac{E\delta}{1-\upsilon^2}\left(\varepsilon_\varphi + \nu\varepsilon_x\right) = \dfrac{E\delta}{1-\upsilon^2}\left(-\dfrac{w}{R} + \nu\dfrac{du}{dx}\right) \end{cases}. \tag{3}$$

With the load of P_x applied, the basic differential equation of the symmetrically loaded cylinder can be written as

$$\frac{d^4w}{dx^4} + 4\beta^4 w = \frac{P_x}{D} + \frac{\nu}{RD}N_x, \tag{4}$$

where

$$\beta = \left(\frac{E\delta}{4R^2D}\right)^{\frac{1}{4}}, D = \frac{E\delta^3}{12(1-\upsilon^2)}. \tag{5}$$

The general solution of the constant coefficients equation is

$$w = e^{\beta x}(C_1\cos\beta x + C_2\sin\beta x) + e^{-\beta x}(C_3\cos\beta x + C_4\sin\beta x) + f(x), \tag{6}$$

in which $f(x)$ is a particular solution of Equation (4) and C_1 to C_4 are the constants of integration that need to be determined in each special case by the conditions at the cylinder ends.

The forces and moments for w are

$$\left.\begin{array}{c} N_\varphi = -E\delta\dfrac{w}{R} + \nu N_x \\ M_x = -D\dfrac{d^2w}{dx^2} \\ M_\varphi = \upsilon M_x \\ P_x = -D\dfrac{d^3w}{dx^3} \end{array}\right\}. \tag{7}$$

Both the base and the pipe can be considered long cylinders and subject to the radial external load, P_x, which is symmetrically distributed about the cylinder central line. Fixing the origin in the cross-section where P_x is applied, the constants of Equation (6) are

$$C_1 = C_2 = 0, C_3 = -\frac{1}{2\beta^3 D}\left(\beta M_0 + \frac{P_x}{2}\right), C_4 = \frac{M_0}{2\beta^3 D}, \tag{8}$$

and the radial deflection w can be derived as

$$w = \frac{e^{-\beta x}}{2\beta^3 D}\left(\beta M_0(\sin\beta x - \cos\beta x) + \frac{P_x}{2}\cos\beta x\right). \tag{9}$$

Then, the deflection, slope, shearing load, and bending moment can be rewritten as

$$\left.\begin{aligned} w &= \frac{P_x}{8\beta^3 D}e^{-\beta x}(\cos\beta x + \sin\beta x) \\ \frac{dw}{dx} &= -\frac{P_x}{4\beta^2 D}e^{-\beta x}\sin\beta x \\ M_x &= \frac{P_x}{4\beta}e^{-\beta x}(\cos\beta x - \sin\beta x) \\ Q_x &= -\frac{P_x}{2}e^{-\beta x}\cos\beta x \end{aligned}\right\}. \tag{10}$$

According to Equation (9), the influenced axial range of the cylinder can be predicted as

$$\left.\begin{aligned} \chi_{p+} &= \frac{3}{4}\pi\left(\frac{E_p\delta_p}{4R_p^2 D_p}\right)^{-\frac{1}{4}} \\ \chi_{p-} &= -\chi_{p+} \end{aligned}\right\}. \tag{11}$$

The half of the 2D axisymmetric connector–pipe assembly with the radial equivalent load, P_z, of the press ring is shown in Figure 3 with regard to the symmetry about the central plane of the connector. The axial distance of the ridge and the anchor is much greater than the half influence range, $L_1 \gg \chi_{p+}$; hence, the coupling effect between the ridge and the anchor can be neglected in the following analysis. In the fitting process, the applied equivalent load, P_z, can be divided into two components: one is for eliminating the maximum radial clearance, h, and the other is for compressing the ridge into the pipe. Meanwhile, the ridge is subjected to the reaction load, P_r, of the pipe. Due to the wedge surfaces inside the press ring, there is a short axial distance, L_0, between P_z and P_r.

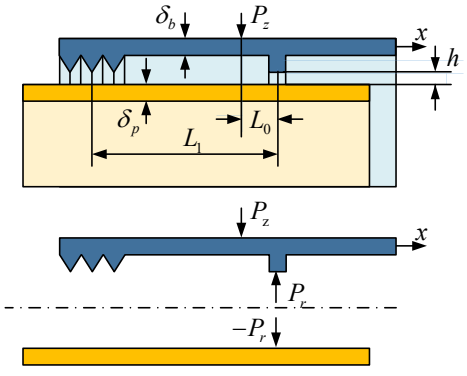

Figure 3. Free-body diagram of the assembly subjected to the radial equivalent load, P_z.

When $\psi(\beta_b x) = e^{-\beta_b x}(\cos\beta_b x + \sin\beta_b x)$, the deflection of the mid-surface of the cylindrical base, w_{b1}, in the radial direction can be expressed as

$$\left.\begin{aligned} w_{b1}(x) &= \frac{P_{b1}}{8\beta_b^3 D_b}\psi(\beta_b x) \\ w_{b1}(L_0) &= h \end{aligned}\right\}. \tag{12}$$

When $\chi_0 = \beta_b L_0$, P_{b1} can be rewritten as:

$$P_{b1} = \frac{8\beta_b^3 D_b}{\psi(\chi_0)} h. \tag{13}$$

Once the ridge contacts the pipe surface, a sealing pressure occurs on the pipe surface. When the pressure reaches the pipe's elastic limit, σ_{sp}, the reaction load, P_r, can be given as

$$P_r = \zeta \sigma_{sp}. \tag{14}$$

In this case, according to the Equation (10), the pipe deflection is

$$w_p(0) = \frac{P_r}{8\beta_p^3 D_p}. \tag{15}$$

The deflection of the base is

$$w_r(0) = \frac{1}{8\beta_b^3 D_b}(P_{b2}\psi(\chi_0) - P_r). \tag{16}$$

Substituting P_r from Equation (15) into Equation (16) yields

$$P_{b2} = \left(\frac{1}{\beta_b^3 D_b} + \frac{1}{\beta_p^3 D_p}\right)\frac{\beta_b^3 D_b}{\psi(\chi_0)} P_r. \tag{17}$$

The total equivalent load on the base is

$$P_z = \frac{\beta_b^3 D_b}{\psi(\chi_0)}\left[8h + \left(\frac{1}{\beta_b^3 D_b} + \frac{1}{\beta_p^3 D_p}\right) P_r\right]. \tag{18}$$

Finally, the deflection can be rewritten as

$$w_x(x) = \left[h + \frac{1}{8}\left(\frac{1}{\beta_b^3 D_b} + \frac{1}{\beta_p^3 D_p}\right) P_r\right]\frac{\psi(\beta_b|x|)}{\psi(\chi_0)} - \frac{P_r}{8\beta_b^3 D_b}\psi\big(\beta_b(|L_0 - x|)\big). \tag{19}$$

In particular, the radial deflection at the point of P_z is

$$w_x(0) = \left[h + \frac{1}{8}\left(\frac{1}{\beta_b^3 D_b} + \frac{1}{\beta_p^3 D_p}\right) P_r\right]\frac{1}{\psi(\chi_0)} - \frac{P_r}{8\beta_b^3 D_b}\psi(\chi_0). \tag{20}$$

The bending moment and slope can also be derived with the same method. Multiple ridges can be designed according to the superposition principle.

3.2. Numerical Modeling and Validation

The finite element method (FE) can be used in the design of the compression connector. In order to validate the proposed macroscopic analytical solutions, a macroscopic 2D axisymmetric FE model is created for the simulation using ABAQUS®/Standard [34].

The base and pipe are idealized as cylinders with a given thickness. An isotropic bilinear hardening model (BISO) with von Mises yield criterion[35] is adopted in which the yield plateau is ignored. The constitutive relationship of the plastic stage takes the form of

$$\sigma^T = \sigma_s + \xi \cdot \varepsilon^T, \tag{21}$$

where σ^T is the true stress, σ_s is the yield strength, and ε^T is the accumulated plastic strain. ξ is the hardening modulus, which can be determined by the tangent modulus, E_t, and Young's modulus, E, with the relation of

$$\xi = \frac{E_t E}{E - E_t}. \tag{22}$$

For general applicability, E_t is averaged and rounded to 5.0 × 10^2 MPa by referring to the properties of wildly used pipe steels: mild steels, Q235, X60, X70, and X80. The geometrical parameters and material properties used in the paper are listed in Table 1.

Table 1. Geometrical parameters and material properties.

Name	Unit	Symbol	Value	
			Base	Pipe
Type	-	-	6-inch	DN 150
Radius	mm	R_b, R_p	215	168
Thickness	mm	δ_b, δ_p	20	20
Yield strength	MPa	σ_{sb}, σ_{sp}	600	235
Axial distance	mm	L_0	0.2	
Radial clearance	mm	h	0.4	
Young's modulus	MPa	E_b, E_p	2.10 × 10^5	
Tangent modulus	MPa	E_t	5 × 10^2	
Poisson coefficient	-	υ	0.3	
Friction coefficient	-	μ	0.2	

The FE model is shown in Figure 4. To consider the large mesh distortion without twist, the four-node bilinear axisymmetric quadrilateral element with reduced integration and hourglass control (CAX4R) is used. The mesh sensitivity is examined. The right corners of the base and the pipe are fixed.

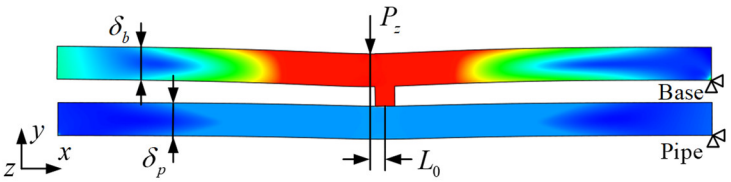

Figure 4. Macroscopic 2D axisymmetric FE model of the assembly.

Between the analytical solution and the FE model, a realistic assumption should be made. Because the analytical solution satisfies the Kirchhoff's hypotheses, one of the hypotheses is that the thickness of the cylinder, δ, is much smaller than the radius of the mid-surface, R (the threshold is $\delta/R \leq 0.05$). In practice, the δ_p/R_p of some pipes is higher than 0.05, e.g., for six-inch pipes, the range is $\delta_p/R_p \in [0.04, 0.54]$ (ASME B36 10M [36] and 19M [37]). To satisfy the maximum mean error of less than 10% between the analytical model and the FE model, in this study, it is assumed that the pipe thickness in the FE simulation is within five times the thin wall threshold; hence, $\delta_p = 20$ mm and $\delta_p/R_p \approx 0.25$. During the macroscopic FE analysis, an equivalent radial external load, P_z, is applied on the appropriate width of the external surface of the base part and is gradually loaded from one to two times the theoretical threshold. The mid-surface deflections of both the base, w_x, and the pipe, w_p, are observed, as shown in Figure 5.

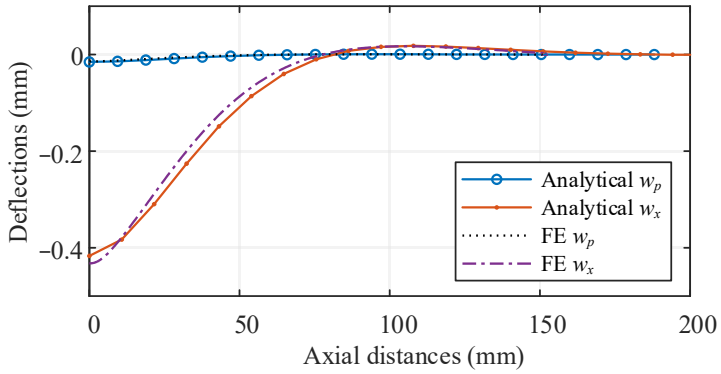

Figure 5. Comparison between the analytical and FE results.

The deflections of the analytical method are consistent with the FE results. In the axial direction, the mean error of w_x with the analytical method is 8.5% compared to that of the FE method, and the mean error of w_p is 5.7%. The error should usually be within 10% [38]. In particular, within an axial distance of 20 mm from the seal (at $x = 0$), the mean error of w_x is only 3.7%. However, the corresponding error of w_p is much higher due to the local plastic deformation on the sealing surface under mesoscopic interference. With the help of a mesoscopic FE model, the sealing process can be analyzed, as discussed in Section 4.

4. FE model of the Sealing Surface

In this section, a mesoscale FE model is created to examine the plastic deformation of the internally turned surface during the fitting process.

4.1. Characterization of the Sealing Surface

The turning process is widely used in the manufacturing of flange surfaces, and these surfaces usually reveal spiral morphology [11,39]. Similarly, due to the difficulty of polishing a thin-walled cylindrical shell [40], the topography produced by the rough turning process is usually left on the ridge surface. The surface was observed using scanning electron microscopy (SEM), as shown in Figure 6.

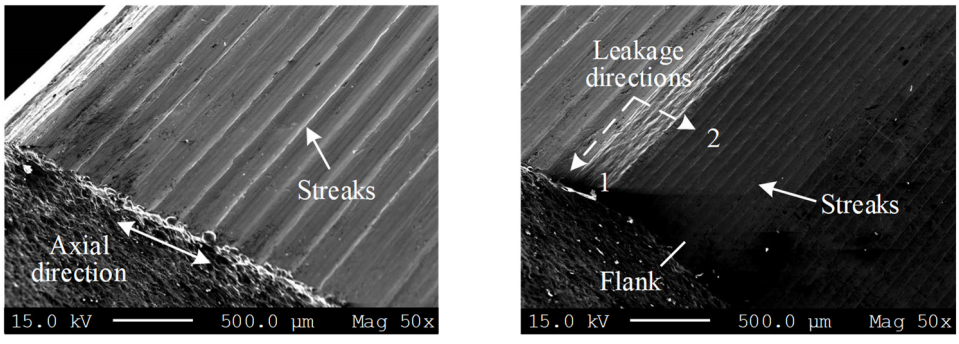

(**a**) (**b**)

Figure 6. Observation of ridge surfaces with SEM: (**a**) sealing surface and (**b**) flank surface.

The internally turned surface has a distinctive anisotropic topography, which is characterized by regular helical and continuous streaks with slight defects and irregularities. Therefore, there are two potential leakage paths: the first one (Direction 1) is the longest helical path along the streak, and the second (Direction 2) is the shortest leak path in the axial direction.

4.2. FE model of the Sealing Surface

According to the turning topography [41,42] and ISO recommendations (ISO 16610-41 [43] and 16610-85 [44]), the surface profile can be considered a periodic connection from the nose profile of the turning tool. Consistently with the SEM results, the mesoscale sealing surface profile is created, as shown in Figure 7.

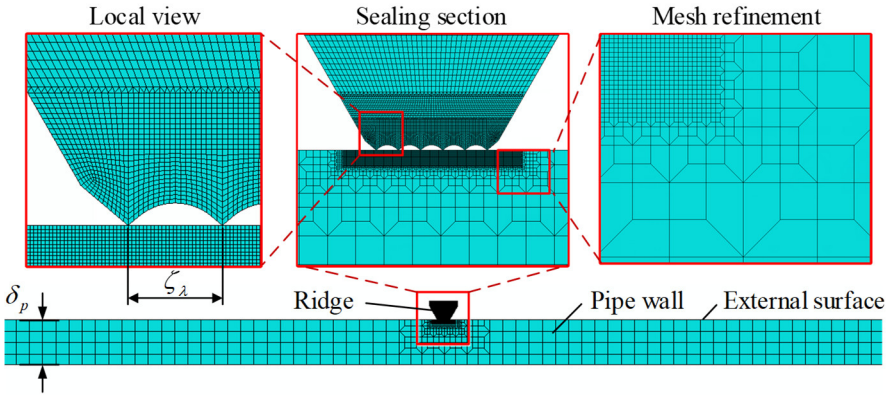

Figure 7. The mesoscale 2D axisymmetric FE model of the seal and local mesh views.

The turning process produces a helical profile on the inner surface in 3D. Chen and Shih [45] have demonstrated that the 2D axisymmetric model can be used to reduce the computational complexity of the helical 3D model while meeting the accuracy requirement. Therefore, a 2D axisymmetric FE model is used. According to Saint-Venant's principle [46], the computation domain is limited to the localized contact region with a portion of the base and is set as $L_0 = 0$ mm. On the sealing surface, since leakage is more of a concern than stress concentration, a groove is positioned at the center and streaks are arranged at both ends. The topography layout is set to an acceptable minimum arrangement of six streaks with five equally spaced grooves. The cross-section of the groove is assumed to be part of a constant circle according to the ISO recommendation. For consistency, additional FE parameters are inherited from the previous macroscopic FE model (in Section 3.2). Since the pipe surface is preprocessed before connection, the surface roughness is 1–2 orders of magnitude smaller than the ridge, and it is simplified to an even surface (no roughing) in the analysis. To show subtle deformation and reduce computation, the mesh is optimized. The sensitivity of the mesh is examined. The following parameters for the study case are provided: the groove radius, $r_c = 0.3$ mm; the pitch of the streaks, $\zeta_\lambda = 0.5$ mm; the sealing width, $\zeta = 3$ mm.

4.3. Change Laws of the Leakage Channel

The interference can be obtained by applying an equivalent deflection/displacement to the ridge in the simulation. According to the FE simulation, the stress contour plots for the corresponding deformation phases are shown in Figure 8a. The deflections of the pipe surface, w_s, the pipe mid-surface, w_p, the streaks, w_k, and the embedded depth of the streaks, h_b, are plotted in Figure 8b. The contact pressure on the sealing surface is shown in Figure 8c.

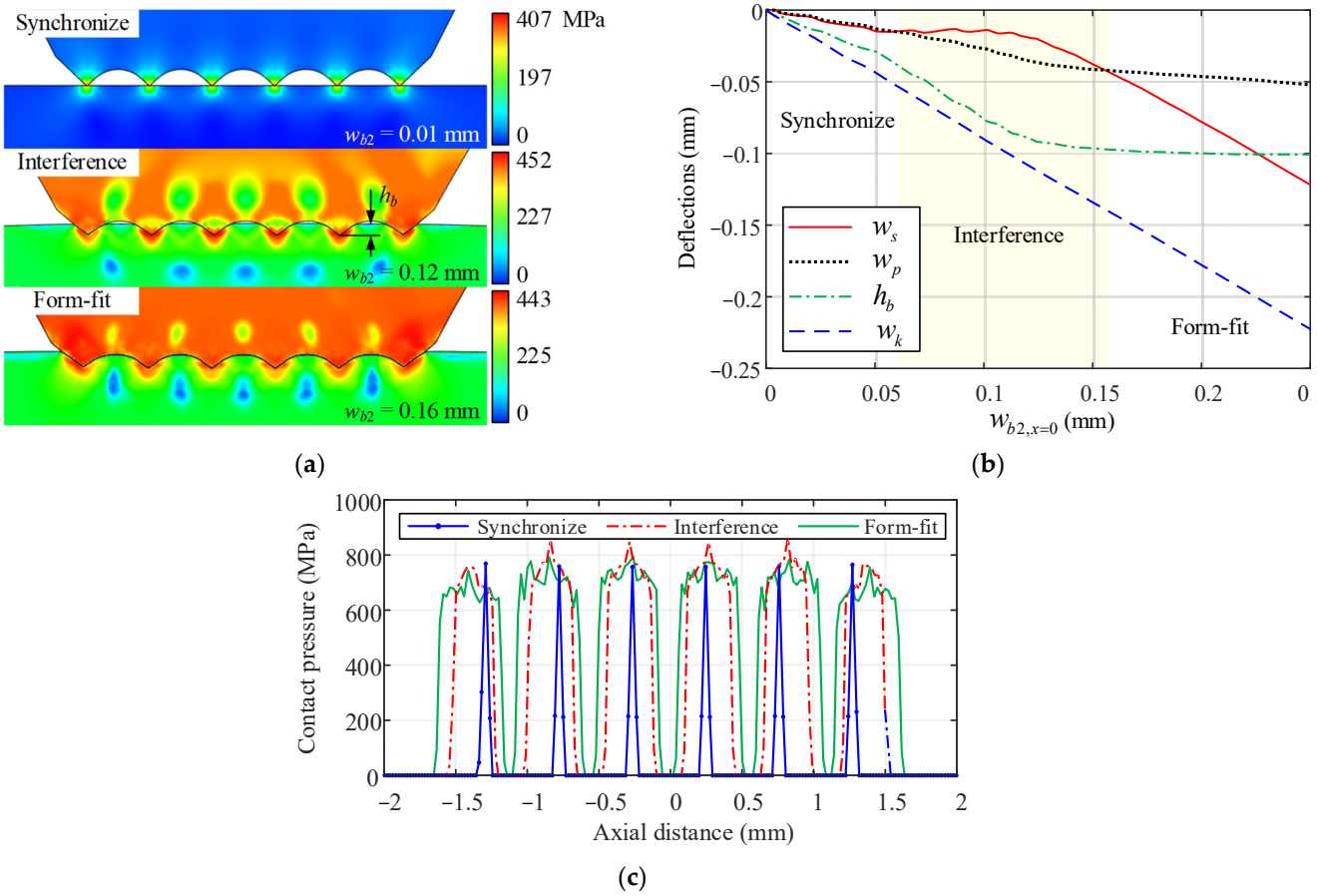

Figure 8. (**a**) Stress contour plots of corresponding deformation phases; (**b**) deflections and embedded depth of the streaks as a function of w_{b2}; (**c**) contact pressure on the sealing surface.

As shown in Figure 8a, both of the streaks of the ridge and the pipe surface are deformed during interference. The local upheaval of the pipe surface further fills the grooves and leads to the change in the cross-section of the leakage channels.

As shown in Figure 8b, the deflection of the pipe surface, w_s, which is distinct from other deflections, has a plateau phase during the embedding, and correspondingly, the embedded depth, h_b, levels off just at the end of the plateau. Hence, the plateau indicates the interference process. The process can be divided into three phases: synchronous (in this case, $w_{b2} \in (0, 0.06)$), interference ($w_{b2} \in (0.6, 0.16)$), and form-fit ($w_{b2} > 0.16$).

As shown in Figure 8c, the contact pressure is distributed axially with stress concentration areas (corresponding to streaks) and untouched areas (corresponding to the helical leakage channel).

The following change laws can be obtained:

- In the synchronize phase, the ridge and pipe deflect synchronously, the streaks are barely embedded in the pipe surface, and the stress concentration occurs at the contact points. Materials are not yielded;
- In the interference phase, streaks continue to be embedded in the pipe surface, the helical leakage channel is narrowed by the plastic deformations of the pipe, and the equispaced contact areas with high-contact pressure extend in the axial direction;
- In the form-fit phase, embedding is mainly performed with constant h_b; however, the plastic deformation of the seal area (the difference between w_s and w_p) continually increases as w_{b2} increases, which makes the seal tighter. The untouched areas narrow considerably and will eventually disappear with the increase in w_{b2}.

To verify the availability of the mesoscale FE model, the analytical values and the mesoscale FE results need to be compared. For w_x, the analytical preload value is 1.35 ×

10^{-2} mm, while the FE range in Figure 8a is from 1.20 × 10^{-2} to 1.40 × 10^{-2} mm; for w_p, the analytical value is 1.54 × 10^{-2} mm, while the FE range is from 0.26 × 10^{-2} to 3.66 × 10^{-2} mm. Therefore, the analytical variables of both the base and the pipe are included in the mesoscale FE model. The availability of the FE model is verified.

5. Semi-Analytical Model of the Leakage

In this section, the leakage ratio is derived from the macroscopic analytical model and the mesoscopic FE model using the Abbott–Firestone curve.

According to the FE results in Section 4.3, the leakage channel and the relevant dimensions are shown in the Figure 9. The height of the leakage paths in the radial direction is h_a, and the embedded depth of the streaks is h_b. Since the axial leakage vanishes during the interference, the direction of the leakage (in Section 4.1) is different before and after the interference [11,47]. Therefore, for the compression connector, the leakage ratio of the helical leak dominates and the boundary condition is limited to radial clearance $h(w_x) < h_a$.

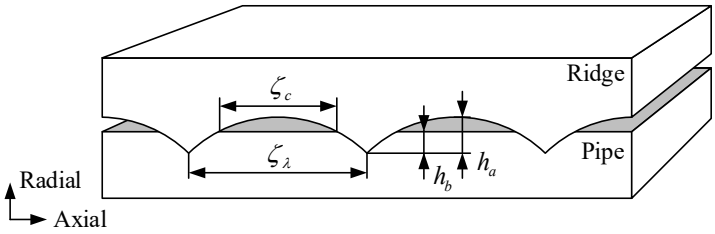

Figure 9. Illustration of the helical streaks embedding into the pipe surface.

To attribute the mesoscale profile parameters for calculating the seal leakage ratio, the Abbott–Firestone curve [48] is used. The effectiveness of the curve has been proved in describing the turning surface. The curve is shown in Figure 10.

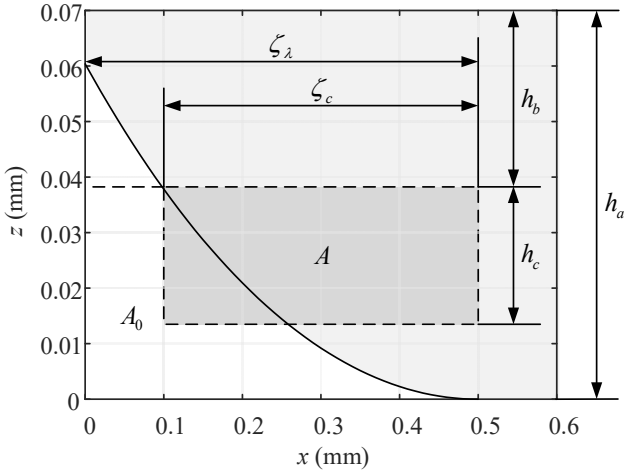

Figure 10. The Abbott–Firestone curve of the sealing surface.

The mathematical formula of the Abbott–Firestone curve can be represented by *z(x)*, which can be mathematically acquired by the fitting method of a polynomial. However, according to the geometric characteristics of the FE model and the parameters in Table 1, $z(x)$ can be given as

$$\frac{1}{4}(\zeta_\lambda - x)^2 + z^2(x) = r_c, x \in (0, \zeta_\lambda). \quad (23)$$

A hypothetical 3D rectangular channel can be used as the leakage path in the mathematical model to calculate the leakage ratio, as shown in Figure 11.

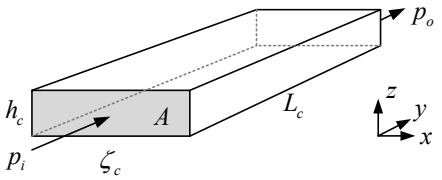

Figure 11. Hypothetical rectangular leakage channel.

The equivalent dimensions are width ζ_c, height h_c and length L_c, of which ζ_c and h_c are regarded as definite values along L_c. A represents the cross-sectional area of the hypothetical rectangular channel. Given the uncertainty of the pressure, the magnitude of the inlet pressure, p_i, and the outlet pressure, p_o, is assumed as $p_i \geq p_o$.

The integral value of the cross-sectional area of the streaks A_o is

$$A_o = \int_0^{\zeta_\lambda} z(x)\, dx. \tag{24}$$

Subjected to $h(w_x)$, the true cross-section of the leakage channel can be calculated by the following relations:

$$A = \zeta_\lambda\big(h_a - h_b(w_x)\big) - A_0. \tag{25}$$

The equivalent height of the leakage channel can be expressed as

$$h_c(w_x) = \frac{A}{\zeta_c(w_x)}. \tag{26}$$

The radius of the leakage path is given by

$$R_c = R_p + \frac{\delta_p + h_a - h_b(w_x)}{2} - w_x. \tag{27}$$

The length of the leakage channel can be defined as

$$L_c = 2\pi R_c\left(\frac{\zeta}{\zeta_\lambda} - 1\right). \tag{28}$$

The governing equation of the flow field based on the laminar flow can be defined using the Reynolds equations [49]:

$$\begin{aligned} &\nabla \cdot (\vec{q}_v) = 0.; \vec{q}_v = -\frac{h^3}{12\eta}\Delta p; \\ &p = p_i, \qquad at\ x = x_i; \\ &p = p_o, \qquad at\ x = x_o, \end{aligned} \tag{29}$$

where $\vec{q}_v$ is the volume flow ratio per unit width, η is the viscosity of the fluid, and p is the fluid pressure. The circumferential leakage ratio, Q_c, can be represented in the following form:

$$Q_c = \int_0^{\zeta_c}\int_0^{h_c} \frac{1}{2\eta}\frac{dp}{dy}(z^2 - h_c z)dz\, dx. \tag{30}$$

The leakage ratio, Q_c, as a function of the radial deflection, w_x, is given as:

$$Q_c(w_x) = \frac{(p_i^2 - p_o^2)\zeta_c(w_x)h_c(w_x)^3}{24\eta L_c p_o}. \tag{31}$$

The following equation introduces the notation:

$$K = \frac{(p_i^2 - p_o^2)}{24\eta L_c p_o}, \qquad J(w_x) = \zeta_c(w_x) h_c(w_x)^3. \tag{32}$$

The leakage ratio can be represented in the simplified form:

$$Q_c(w_x) = K \cdot J(w_x). \tag{33}$$

6. Results and Discussion

6.1. Parameter Analysis

The proposed semi-analytical method can reveal the relationship between the deflection and the leakage condition. Therefore, the key parameters are those that have an impact on the relationship as they influence deflection and are easy to implement in design. Via multi-scale parameter analysis, key design and performance rules can be identified, and the minimum preloaded deflection can be obtained.

On the macroscopic level, the effects of the radius and clearance on deflections are first investigated. Because R_b is determined by R_p, δ, and h, by taking R_p as an independent variable while others are constant, the influences of R_p on w_x and w_p at $x = 0$ are plotted with logarithmic coordinates using Equations (15) and (20), as shown in Figure 12a. However, according to Equations (12) and (13), h is positively correlated with the deflection component, w_{b1}, and its influence on the total deflection, w_x, varies. As a reference for the design, with the increase in h, the corresponding change in h/w_x and its gradient is calculated, as shown in Figure 13b. Note that w_p is not shown in Figure 12b since it is irrelevant to h from Equation (15).

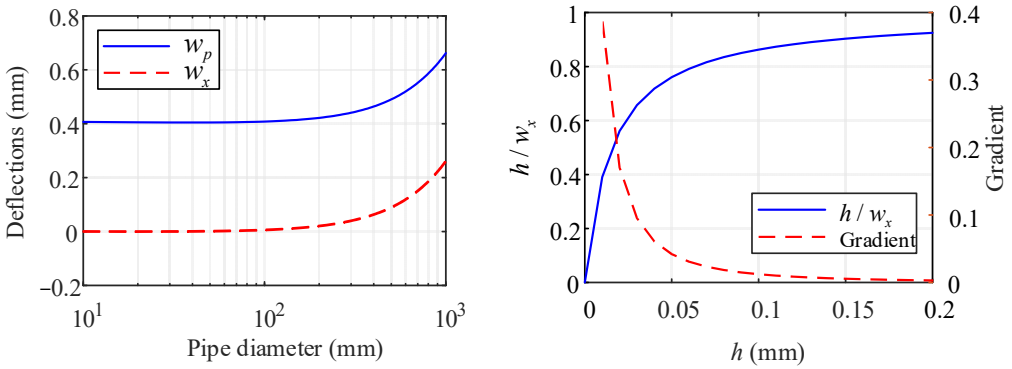

Figure 12. (**a**) Deflections as a function of pipe diameter and (**b**) ratio h/w_x as a function of radial clearance, h, at $x = 0$.

The following conclusions are drawn from Figure 12a:

- Compared to w_p, pipe diameter shows almost exact influence trends on w_x; hence R_p is positively correlated with both deflections;
- For all standard diameters in the ratio range of $\delta_p/R_p < 0.25$, within four-inch diameters ($R_p \leq 50$ mm), changes of w_x and w_p can be considered independent of R_p.
- The following conclusions are drawn from Figure 12b:
- The increment of w_x is gradually related to h, and, in this instance, when $h > 0.2$ mm, the gradient of h/w_x approaches zero;
- There is a threshold of h (when $h = 0.2$) at which the growth of w_x is directly proportional to the growth of h.

Similarly to the radius, R, the thickness, δ, also shows a prominent influence on the deflections. The thickness of the base, δ_b, and the pipe, δ_p, are analyzed under three conditions: in Case 1, δ_b is constant and δ_p is variable; Case 2 has the opposite conditions to

Case 1; in Case 3, $\delta_b = \delta_p$ is considered. Note that, according to Equation (15), δ_b is irrelevant to w_p. The influences of δ on the deflections are shown in Figure 13. The curve in Case 1 (w_x) is the influence of δ_p on w_x while δ_b = 20 mm, and the w_p in Case 1 is the influence on w_p. The w_x in Case 2 is the influence of δ_b on w_x while δ_p = 20 mm. The w_x in Case 3 is the influence of δ_p on w_x while $\delta_b = \delta_p$, and the w_p in Case 3 is the influence on w_p.

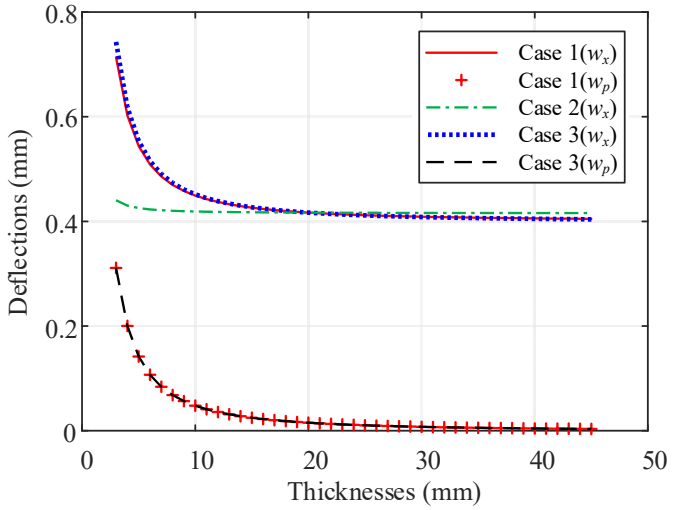

Figure 13. Deflections as a function of thickness at x = 0.

The following conclusions are drawn from Figure 13:

- As the δ_p increases, all deflections decrease with a decreased change rate;
- δ_b has a minimum influence on w_x (the curve w_x in Case @), and is irrelevant to w_p, so the change in δ_b has a negligible impact on the interference. Therefore, consideration may be given to appropriately increasing or decreasing the thickness, δ_b, as needed.

In addition to the above parameters, deflections are also affected by the sealing width. For generality, a ratio of the pipe thickness to the sealing width, δ_p/ζ, is used. The deflection as a function of δ_p/ζ is shown in Figure 14 with logarithmic coordinates. Moreover, since the ratio also affects flexural rigidity, the flexural rigidity of the pipe, D_p, is also shown in the figure.

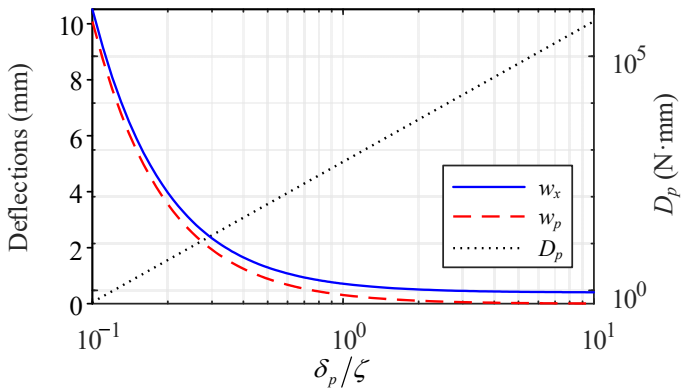

Figure 14. Deflections as a function of ratio δ_p/ζ.

As shown in Figure 14, deflections and D_p have different responses:

- For the flexural rigidity, a linear relationship exists between the ratio and D_p in logarithmic coordinates;
- For deflections, they are influenced by a threshold of the ratio: when $\delta_p/\zeta \leq 1$, deflections decrease as the ratio increases; when $\delta_p/\zeta > 1$, the deflection change is practically unrelated to the ratio. This shows that when the thickness exceeds the sealing width, δ_p/ζ hardly affects deflection.

Next, the effects of D_b and D_p on deflections are also investigated as depicted in the logarithmic coordinates in Figure 15. Since w_p is irrelevant to D_b, its curve is not shown.

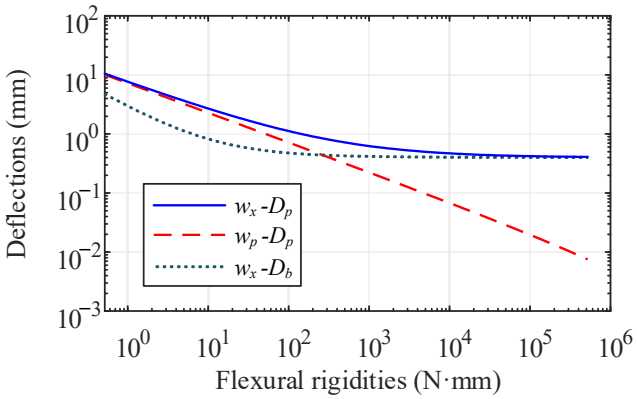

Figure 15. Deflections as a function of flexural rigidities.

As shown in Figure 15, D_p exhibits distinct effects on w_p and w_x:

- D_p exhibits an almost linear relationship with w_p (the curve w_p-D_p) in logarithmic coordinates but a decreasing effect on w_x (w_x-D_p);
- When $D_p < 10^3$, all effects on deflections are approximately linear, but when $D_p \geq 10^3$, the effect on w_x and w_p is significantly different;
- When $D_p \geq 10^4$, the only effect of the flexural rigidity is that of D_p on w_p;
- The effect on w_x of the flexural rigidity of D_b (w_x-D_b) is comparable to that of the pipe (w_x-D_p).

On the mesoscopic level, the leakage condition can be analyzed. The influence of w_x on the nonlinear change in the cross-sectional area of the leakage channel A is investigated first. Based on the mesoscopic FE model (in Section 4), the true width, ζ_c, and the equivalent height, h_c, of A are shown in Figure 16 with w_x increments, where the corresponding radius of the leakage path, R_c, is also depicted to indicate the relationship between macroscopic and mesoscopic changes.

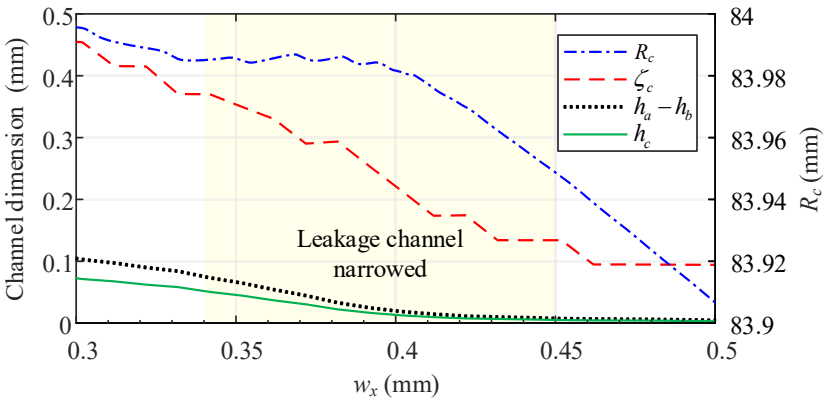

Figure 16. Leakage channel dimension and sealing radius as a function of base deflection.

The following conclusions can be drawn from Figure 16:

- There is a strong correlation between w_x and ζ_c: as w_x increases, both ζ_c and h_c decrease;
- Coincidentally with the macroscopic results in Section 4.3, the true height of the channel $(h_a - h_b)$ and h_c also have a notable reduction during the interference within the range $w_x \in (0.34, 0.45)$, while h_c shows a clear descent stage;
- When $w_x > 0.45$ mm, ζ_c and h_c are virtually unchanged, indicating that the leakage ratio is stable.

Based on the above findings, the minimum preloaded deflection can be predicted. Since Q_c varies with different sealed mediums, the typical leakage ratios of water ($\eta = 1.77 \times 10^5$ Pa·s), air ($\eta = 1.01 \times 10^3$ Pa·s), and oil ($\eta = 1.50$ Pa·s), with inlet pressure, $p_i =$ 1 MPa, and outlet pressure, $p_o = 101$ KPa, can be calculated as a function of w_x, as shown in Figure 17 in the logarithmic coordinates. The corresponding R_c is also shown. Other unlisted parameters are consistent with the above analyses.

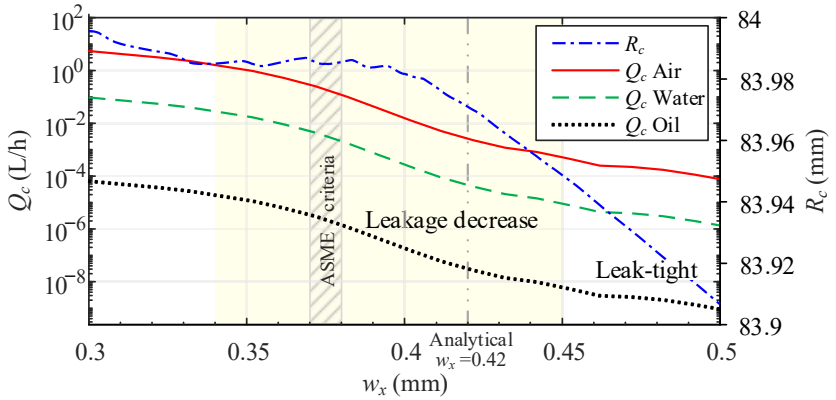

Figure 17. Leakage ratios as a function of base deflection.

As shown in Figure 17, the air leakage ratio is distinct from other mediums, which makes a great difference to the sealing performance of connectors. Accordingly, the following conclusions are drawn:

- For air medium, according to the highest Class VI of ASME B16.104 [50], the connector can be considered leak-tight below, $Q_c = 0.24$ L/h in the study case, while the corresponding minimum w_x is in the range from 0.37 to 0.38 mm (0.25 to 0.10 L/h, shadowed area in the figure);
- Similar to the equivalent height curve, h_c, in Figure 16, there is also an accelerated descent range of the leakage ratio and all leakage ratios are reduced to a minimum with $w_x > 0.45$ mm;
- The macroscopic minimum, w_x, calculated from the proposed analytical model is 0.42 mm (the dash-double-dotted line in the figure), which is covered by the ASME criteria;
- The ASME criteria and the theoretical minimum, w_x, are included within the leakage decrease range (from 0.37 to 0.45). Therefore, the results of the semi-analytical method are self-consistent, and the case connector is theoretically leak-tight to all typical mediums. The theoretical feasibility of the proposed semi-analytical method to predict the minimum preloaded deflection is verified.

At the end of the parameter analysis, considering the negligible effect of the thickness, the leakage ratio as a function of the rate, δ_p/ζ, is explored in Figure 18 with logarithmic coordinates. The corresponding R_c and ASME criteria of the air leakage ratio (from 0.53 to 0.20 L/h, shadowed area in the figure) are also shown.

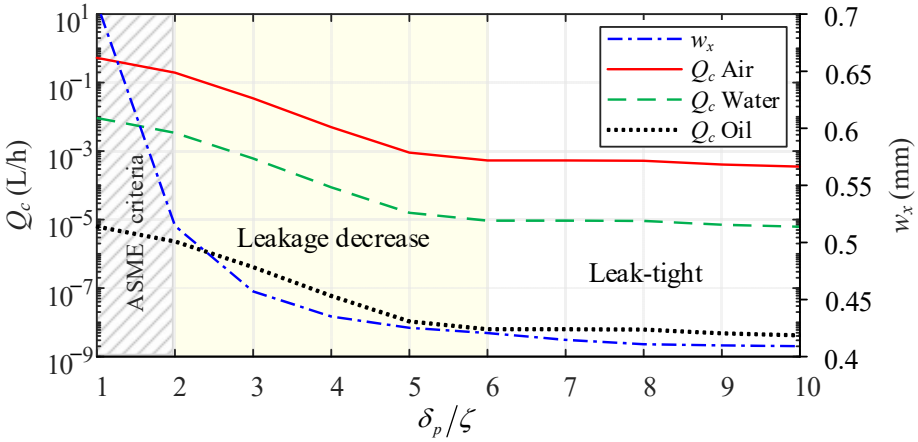

Figure 18. Leakage ratios as a function of rate δ_p/ζ.

The following conclusions can be drawn from Figure 18:

- When $\delta_p/\zeta \in (1, 3]$, w_x and Q_c begin descending with the increase in δ_p/ζ;
- When $\delta_p/\zeta \in (3, 5]$, the leakage is noticeably decreasing;
- When $\delta_p/\zeta > 5$, the effects on w_x, Q_c, and r_c are moderated, the leakage is stable, and the sealing state needs to be further verified by prototype tests;
- When $\delta_p/\zeta \leq 3$, the leakage may occur on the internally turned topography, the recommended design value is $\delta_p/\zeta \geq 5$.

6.2. Experimental Test

In order to verify the feasibility of the proposed semi-analytical method on the sealing performance prediction, according to ISO 21329:2004 [51], a working pressure test and a burst pressure test are carried out. All tests are conducted under the temperature of 25 °C and the maximum gauge pressure is 60 MPa with an accuracy rating of 0.4 (0.24 MPa). Furthermore, a customized 80 MPa manual hydraulic pump and an air compressor are used. The schematic diagram of the experimental setup is shown in Figure 19.

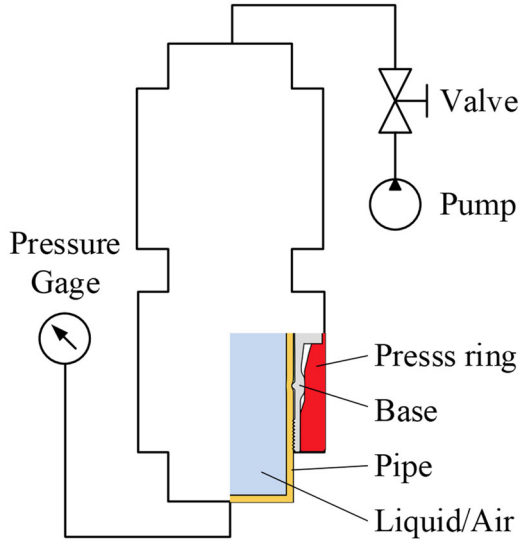

Figure 19. Schematic diagram of the experimental setup.

Prototypes are developed based on the proposed semi-analytical approach using seamless wrought steel pipes (ASME B36 10M [36]) of 3 to 8 inches. Geometrical parameters are listed in Table 2. A few redesigned prototypes are shown in Figure 20.

Table 2. Geometric and material parameters for prototype types.

Type		Nominal Diameter	Nominal Thickness	Medium		Yield Strength (MPa)	
DN	Inch	(mm)	(mm)	Water	Air	Pipe	Connector
80	3	89	5	15	0.2	235	345
100	4	114	7	7	0.1		
150	6	168	8	6	0.1		
200	8	219	10	4.5	0.08		

(**a**) (**b**)

Figure 20. Prototypes: (**a**) DN 200 type and (**b**) DN 100 type.

6.2.1. Working Pressure Test

The purpose of the test is to verify whether the designed prototype can reach the designed working pressure. The mediums are clean air and water. For the air pressure test, the prototype is pressurized with air at the required depth of an experimental tank. During the working pressure test, the internal pressure gradually increases to the required working pressure, rising below a maximum rate of 100 MPa/min. When the working pressure is reached, to stabilize the system and periodically check the assembly for the leakage it is necessary to maintain constant pressure for a sufficient time (10 min for air pressure and 24 h for hydraulic pressure in the study). Neither structural failure nor visual indications of the leakage are permitted. The setups of the air pressure test and the hydraulic pressure test are shown in Figure 21. A sectional view of the tested prototype is shown in Figure 22.

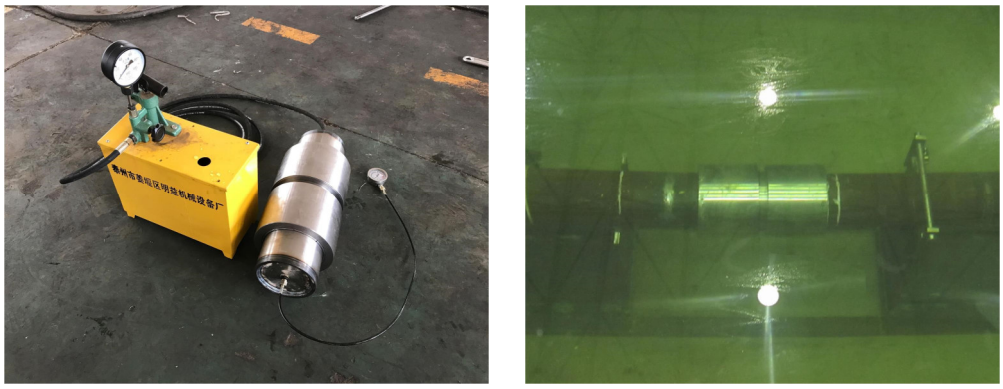

(**a**) (**b**)

Figure 21. Experiment setups with assemblies of (**a**) hydraulic pressure test and (**b**) air pressure test.

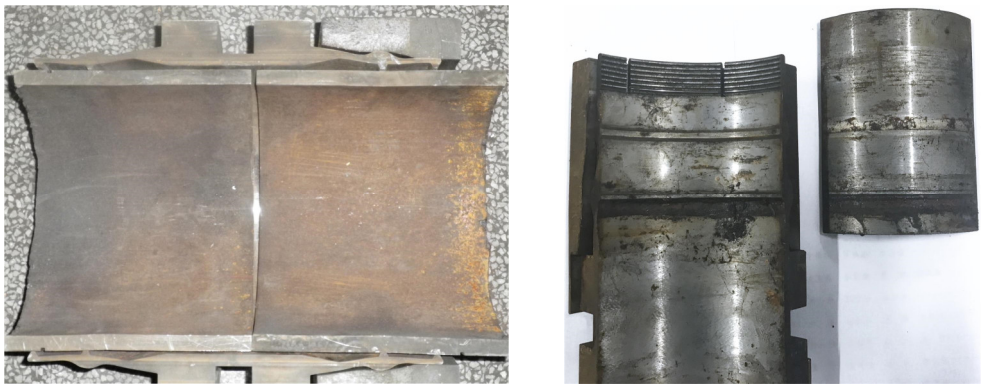

(a) (b)

Figure 22. Section view of assemblies of (**a**) DN 200 and (**b**) DN 80.

From Figure 22, the internal deflection of the prototypes conforms to the design expectation, there are no visual indications of leakage during sampling inspection with different sealing widths under variable structure configurations, and specimens are in good contact with seals. The sealing surface condition is not detailed here since it has already been discussed in our previous studies [20,22].

Typical test results for the prototypes are shown in Table 3, indicating that all prototypes are leak tight. Therefore, the prototypes developed by the proposed semi-analytical method meet the working pressure requirement.

Table 3. Typical results of the working pressure test.

Type		Pressure (MPa)		Pressure Drop		Leakage		Structural Change	
DN	Inch	Water	Air	Water	Air	Water	Air	Water	Air
80	3	15	0.2	×	×	×	×	×	×
100	4	7	0.1	×	×	×	×	×	×
150	6	6	0.1	×	×	×	×	×	×
200	8	4.5	0.08	×	×	×	×	×	×

6.2.2. Burst Pressure Test

The purpose of the test is to find the failure pressure of the designed prototypes. To avoid the risk of the compression air, only the hydraulic pressure was applied. Following the leak test, the pressure is continuously raised below the maximum pressurization rate, and the pressure is maintained for 5 min per 1 MPa until there is evidence of the structural failure or leakage. The mean failure pressures for the prototypes are listed in Table 4. For comparison, the results of the same prototype types with polished sealing surfaces from our previous design by FE methods [20,22] are also listed.

Table 4. Failure pressures of burst test with failure types and comparison with previous designs.

Type		Mean Burst Pressure (MPa)		Pressure Drop	Leakage	Structural Change
DN	Inch	Current	Previous			
80	3	45	36	√	×	√
100	4	33	30	√	×	√
150	6	20	20	×	×	√
200	8	12	10	×	×	√

According to Table 4, there is no significant difference between the analytical design and the previous FE design, indicating that the semi-analytical solution does not have a considerable effect on the previous solution. In addition, the experiments did not show

any leakage. All failures are structural, and most are manifested as the axial pipe movement. In the failure, the internal pressure no longer increased and decreased slightly in some tests. This type of failures involves axial anchoring failure and pull-out deformation, which will be discussed in a follow-up study.

To summarize, the results show that even with a rough radial sealing surface, the compression connector designed by the proposed method can quickly create a reliable radial seal. On the other hand, the computational time has been reduced, saving more than 57% design time in practice. Meanwhile, the internal finish turning machining is no longer necessary, which further reduces the time and cost of the manufacturing process.

7. Conclusions

A semi-analytical method for the sealing performance prediction of the subsea pipeline compression connector is proposed in this paper. Prototypes are fabricated on the basis of the design results with this method and the failure pressures are tested in lab. The following conclusions can be drawn:

An analytical model of the fitting process of the compression connector is derived, based on the membrane theory, in which the assembly is idealized as pairs of thin-walled cylinders under uniformly distributed radial load. The expressions of the deflections with the contact pressure are obtained;

1. A macroscopic 2D FE model is created to verify the analytical model. An agreement is found between the analytical and FE results with a mean error of less than 8.5%. The analytical model is proven to be good enough with the thickness–radius ratio being no more than 0.25 ($\delta/R \leq 0.25$);
2. The geometric parameter effects on the interference process are investigated. The influence and thresholds of the geometric parameters on sealing performance are presented, which provide the design guidance for the subsea pipeline compression connector;
3. The radial sealing surface of the connector is observed by SEM. The surface is an anisotropic topography characterized by regular helical and continuous streaks with slight defects and irregularities. Potential leak paths in two orthogonal directions are identified as axial and circumferential;
4. A mesoscopic 2D FE model is created based on the SEM result and the macroscopic FE model. The effects of the leakage channel in the sealing process are analyzed. Then, the analytical minimum deflections and those of FE are compared and shown to be consistent with each other. Since the macroscopic analytical minimum deflections of both the base and the pipe are included in the mesoscale results, it is theoretically verified that the semi-analytical method can identify and predict the leakage condition of the connector;
5. The Abbott–Firestone curve of the sealing surface is introduced based on SEM observation and the FE model. A semi-analytical leakage model was obtained. Since the true height of the leakage channel shows a clear descent stage, the minimum preloaded deflection of the leak-tight range is identified. On the rough internally turned sealing surface, leakage may occur when the ratio of the pipe thickness to the sealing width is $\delta_p/\zeta < 3$, and the recommended leak-tight design value is $\delta_p/\zeta > 5$;
6. The results with the proposed semi-analytical method correlate well with the working pressure test and the burst pressure test. The designed connectors can quickly create a reliable radial metal static seal with the rough turning topography and save more than 57% of design time compared to the common FE method, while reducing machining time and costs.
7. The proposed semi-analytical method can be used to optimize the overall structural performance of compression connectors with a low computational cost. It allows the prediction and identification of the leakage condition of all standard pipe series with $\delta_p/R_p \leq 0.25$. The model also provides a good understanding of the radial sealing

process. These results are helpful to highlight the different sealing performances with other type of seals and guide the further improvements.

In order to perform further quantitative analyses of the leakage ratio, it is necessary to explore the tangential contact mechanics and the deflection behaviors of the connector in subsequent studies.

Author Contributions: Conceptualization, Z.L., G.W. and L.W.; methodology, Z.L.; software, Z.L.; validation, Z.L. and L.W.; formal analysis, Z.L.; investigation, G.W.; resources, L.W. and C.L.; data curation, G.W. and S.Y.; writing—original draft preparation, Z.L.; writing—review and editing, S.Y.; visualization, Z.L.; supervision, P.J. and F.Y.; project administration, G.W.; funding acquisition, L.W. All authors have read and agreed to the published version of the manuscript. All authors have read and agreed to the published version of the manuscript.

Funding: This research was funded by the National Natural Science Foundation of China, grant number 51779064, 52001089 and the China Postdoctoral Science Foundation, grant number 2020M670889.

Institutional Review Board Statement: Not applicable.

Informed Consent Statement: Not applicable.

Data Availability Statement: The data used to support the findings of this study are included within the article.

Conflicts of Interest: The authors declare no conflicts of interest.

Nomenclature

A	Cross-sectional area of the hypothetical rectangle channel (mm^2)
A_o	Integral value of the total Abbott–Firestone curve (mm^2)
D, D_b, D_p	Flexural rigidity of cylindrical shell, base, and pipe, respectively (N·mm)
E	Young's modulus (MPa)
E_t	Tangent modulus (MPa)
h	Radial clearance between sealing surfaces (mm)
h_a	Height of streaks (mm)
h_b	Depth of embedded streaks (mm)
h_c	Equivalent height of the hypothetical rectangular channel (mm)
L_0	Axial distance between radial load and ridge (mm)
L_1	Axial distance between anchors and ridge (mm)
L_c	Length of the leakage channel (mm)
M_φ, M_x	Bending moments of axial section and a section perpendicular to the axis of a cylindrical shell, respectively (N·mm)
N_φ, N_x	Membrane forces of axial section and a section perpendicular to the axis of a cylindrical shell, respectively (N)
p_i, p_o	Inlet the outlet pressures of the leakage channel (MPa)
P_{b1}, P_{b2}	Components of radial load P_z (N/mm)
P_r	Reaction load (N/mm)
P_x	Shearing force of intensity parallel to z axis of a section perpendicular to the axis of a cylindrical shell (N)
P_z	Total equivalent radial load on the base (N/mm)
Q_c	Helical leakage ratio (L/h)
r_c	Corner radius of the tool nose (mm)
R, R_b, R_p	Radius of mid-surface of cylinder, base, and pipe, respectively (mm)
R_c	Radius of leakage path (mm)
u, v, w	Displacements of the mid-surface in the cylindrical coordinate (mm)
w_{b1}, w_{b2}	Deflection components of P_z (mm)
w_x, w_p	Radial deflection of the base and pipe, respectively (mm)
w_k	Deflection of the streak peaks (mm)
w_r	Deflection component of P_r (mm)
w_s	Deflection of pipe surface at the seal (mm)

x, y, z	Global rectangular coordinates of 2D axisymmetric FE model
$\delta, \delta_b, \delta_p$	Thickness of cylinder, base, and pipe, respectively (mm)
$\varepsilon_\varphi, \varepsilon_x$	Strain components of cylindrical coordinates
ε^T	True strain
ζ	Sealing width (mm)
ζ_c	Width of the leakage channel (mm)
ζ_λ	Pitch of the streaks (feed rate) (mm)
η	Kinematic viscosity (Pa·s)
μ	Friction coefficient
υ	Poisson's ratio
ξ	Hardening modulus (MPa)
σ_{sb}, σ_{sp}	Yield strength of the base and pipe, respectively (MPa)
σ^T	True stress (MPa)
$\varphi, x, \rho(=R+z)$	Cylindrical coordinates

References

1. Yun, F.; Liu, D.; Xu, X.; Jiao, K.; Hao, X.; Wang, L.; Yan, Z.; Jia, P.; Wang, X.; Liang, B. Thermal–Structural Coupling Analysis of Subsea Connector Sealing Contact. *Appl. Sci.* **2022**, *12*, 3194. https://doi.org/10.3390/app12063194.
2. *ASTM F1387*; Standard Specification for Performance of Piping and Tubing Mechanically Attached Fittings. ASTM International: West Conshohocken, PA, USA, 2012.
3. *ISO 8434-1*; Metallic Tube Connections For Fluid Power and General Use Part 1:24° Compression Fittings. International Organization for Standardization: Geneva, Switzerland, 2018.
4. Okada, H.; Itoh, T.; Suga, T. The Influence of Surface Profiles on Leakage in Room Temperature Seal-Bonding. *Sens. Actuators A Phys.* **2008**, *144*, 124–129. https://doi.org/10.1016/j.sna.2007.12.023.
5. Lebeck, A.O. Hydrodynamic Lubrication in Wawy Contacting Face Seals-a Two Dimensional Iodei. *J. Tribol.* **1981**, *103*, 578–586. https://doi.org/10.1115/1.3251742.
6. Matsuzaki, Y.; Kazamaki, T. Effect of Surface Roughness on Compressive Stress of Static Seals. *JSME Int. J. Ser. 3* **1988**, *31*, 99–106. https://doi.org/10.1299/jsmec1988.31.99.
7. Yanagisawa, T.; Sanada, M.; Koga, T.; Hirabayashi, H. The Influence of Designing Factors on the Sealing Performance of C-Seal. *SAE Trans.* **1991**, *100*, 651–657.
8. Nakamura, T.; Funabashi, K. Effects of Directional Properties of Roughness and Tangential Force on Pressure Flow between Contacting Surfaces. *Lubr. Sci.* **1991**, *4*, 13–23. https://doi.org/10.1002/ls.3010040103.
9. Polycarpou, A.A.; Etsion, I. A Model for the Static Sealing Performance of Compliant Metallic Gas Seals Including Surface Roughness and Rarefaction Effects. *Tribol. Trans.* **2000**, *43*, 237–244. https://doi.org/10.1080/10402000008982334.
10. Geoffroy, S.; Prat, M. On the Leak through a Spiral-Groove Metallic Static Ring Gasket. *J. Fluids Eng. Trans. ASME* **2004**, *126*, 48–54. https://doi.org/10.1115/1.1637627.
11. Liao, C.; Xu, X.; Fang, H.; Wang, H.; Man, M. A Leakage Model of Metallic Static Seals Based on Micromorphology Characteristics of Turning Flange Surface. *Ind. Lubr. Tribol.* **2015**, *67*, 572–581. https://doi.org/10.1108/ILT-04-2015-0049.
12. Beheshti, A.; Khonsari, M.M. Asperity Micro-Contact Models as Applied to the Deformation of Rough Line Contact. *Tribol. Int.* **2012**, *52*, 61–74. https://doi.org/10.1016/j.triboint.2012.02.026.
13. Jackson, R.L.; Green, I. On the Modeling of Elastic Contact between Rough Surfaces. *Tribol. Trans.* **2011**, *54*, 300–314. https://doi.org/10.1080/10402004.2010.542277.
14. Marie, C.; Lasseux, D.; Zahouani, H.; Sainsot, P. An Integrated Approach to Characterize Liquid Leakage through Metal Contact Seal. *Eur. J. Mech. Environ. Eng.* **2003**, *48*, 81–86.
15. Liao, Y.; Stephenson, D.A.; Ni, J. Multiple-Scale Wavelet Decomposition, 3D Surface Feature Exaction and Applications. *J. Manuf. Sci. Eng.* **2012**, *134*, 011005. https://doi.org/10.1115/1.4005352.
16. Deltombe, R.; Bigerelle, M.; Jourani, A. Analysis of the Effects of Different Machining Processes on Sealing Using Multiscale Topography. *Surf. Topogr. Metrol. Prop.* **2016**, *4*, 015003. https://doi.org/10.1088/2051-672X/4/1/015003.
17. Bricaud, C.; Schulz, O.; Zierer, T.; Peltier, V.; Schwitzke, C.; Bauer, H.J. Experimental Investigations Into the Effect of Surface Roughness and Contact Force on Leakage Between Two Rigid Metallic Surfaces. *J. Eng. Gas Turbines Power* **2022**, *144*, 061006. https://doi.org/10.1115/1.4053965.
18. Weddeling, C.; Demir, O.K.; Haupt, P.; Tekkaya, A.E. Analytical Methodology for the Process Design of Electromagnetic Crimping. *J. Mater. Process. Technol.* **2015**, *222*, 163–180. https://doi.org/10.1016/j.jmatprotec.2015.02.042.
19. Weddeling, C.; Walter, V.; Haupt, P.; Tekkaya, A.E.; Schulze, V.; Weidenmann, K.A. Joining Zone Design for Electromagnetically Crimped Connections. *J. Mater. Process. Technol.* **2015**, *225*, 240–261. https://doi.org/10.1016/j.jmatprotec.2015.06.009.
20. Wei, Z.; Wang, L.; Guan, Y.; Yao, S.; Li, S. Static Metal Sealing Mechanism of a Subsea Pipeline Mechanical Connector. *Adv. Mech. Eng.* **2016**, *8*, 1–16. https://doi.org/10.1177/1687814016654821.
21. Henriksen, J.; Hansen, M.R.; Thrane, F.C. Axial Load Capacity of Cold Formed Pipe Flange Connection. *J. Press. Vessel Technol.* **2017**, *139*, 051201. https://doi.org/10.1115/1.4036853.

22. Wang, L.Q.; Wei, Z.L.; Yao, S.M.; Guan, Y.; Li, S.K. Sealing Performance and Optimization of a Subsea Pipeline Mechanical Connector. *Chin. J. Mech. Eng. Engl.* **2018**, *31*. https://doi.org/10.1186/s10033-018-0209-6
23. Onyegiri, I.; Kashtalyan, M. Threaded Connectors for Sandwich Pipes—Part 1: Parametric & Comparative Studies. *Int. J. Press. Vessel. Pip.* **2018**, *168*, 117–124. https://doi.org/10.1016/j.ijpvp.2018.09.010.
24. Quispe, J.L.P.; Pasqualino, I.P.; Estefen, S.F.; de Souza, M.I.L. Structural Behavior of Threaded Connections for Sandwich Pipes under Make-up Torque, External Pressure, and Axial Load. *Int. J. Press. Vessel. Pip.* **2020**, *186*, 104156 https://doi.org/10.1016/j.ijpvp.2020.104156.
25. Yan, Y.; Fan, Y. Influence of Fluid on Seal and Assembly of Pipeline Fittings Based on the Multiscale Finite Element Model. *Complexity* **2020**, *2020*, 4960734. https://doi.org/10.1155/2020/4960734.
26. Agrawal, A.K.; Narayanan, R.G. Experimental and Numerical Studies on Joining Steel Tubes by End Forming. *J. Constr. Steel Res.* **2020**, *167*, 105792. https://doi.org/10.1016/j.jcsr.2019.105792.
27. Liu, Z.; Zhang, L.; Wang, F.; Li, S.; Wang, P.; Cai, M.; Han, L.; Ma, Y.; Ma, Z.; Yan, B. Study on Optimization Design of Permanent Packer Slip Structure. *J. Fail. Anal. Prev.* **2020**, *21*, 50–60. https://doi.org/10.1007/s11668-020-01063-w.
28. Wu, L.; Guo, X.; Chen, H.; Liu, J.; Su, Y. Calculation Method for the Axial Load-Bearing Capacity of Steel Pipe-to-Sleeve Grouted Connections. *Constr. Build. Mater.* **2022**, *314*, 125621. https://doi.org/10.1016/j.conbuildmat.2021.125621.
29. Weddeling, C.; Gies, S.; Khalifa, N.B.; Tekkaya, A.E. Analytical Methodology for the Process and Joint Design of Form-Fit Joining by Die-Less Hydroforming. In Proceedings of the ASME 2014 International Manufacturing Science and Engineering Conference, MSEC 2014 Collocated with the JSME 2014 International Conference on Materials and Processing and the 42nd North American Manufacturing Research Conference, Web Portal ASME (American Society of Mechanical Engineers), Detroit, MI, USA, 9–13 June 2014; Volume 2.
30. Ernens, D.; Pérez-Ràfols, F.; van Hoecke, D.; Roijmans, R.F.H.; van Riet, E.J.; Vande Voorde, J.B.E.; Almqvist, A.; de Rooij, M.B.; Roggeband, S.M.; van Haaften, W.M.; et al. On the Sealability of Metal-to-Metal Seals with Application to Premium Casing and Tubing Connections. *SPE Drill. Complet.* **2019**, *34*, 382–396. https://doi.org/10.2118/194146-PA.
31. Weber, F.; Gebhard, J.; Gitschel, R.; Goyal, S.; Kamaliev, M.; Wernicke, S.; Tekkaya, A.E. Joining by Forming–A Selective Review. *J. Adv. Join. Process.* **2021**, *3*, 100054. https://doi.org/10.1016/j.jajp.2021.100054.
32. Orynyak, I.; Bai, Y. Coupled Approximate Long and Short Solutions versus Exact Navier and Galerkin Ones for Cylindrical Shell under Radial Load. *Thin-Walled Struct.* **2022**, *170*, 108536. https://doi.org/10.1016/j.tws.2021.108536.
33. Kumar, A.; Das, S.L.; Wahi, P.; Żur, K.K. On the Stability of Thin-Walled Circular Cylindrical Shells under Static and Periodic Radial Loading. *J. Sound Vib.* **2022**, *527*, 116872. https://doi.org/10.1016/j.jsv.2022.116872.
34. *Abaqus*, Version 6.14; Software for Technical Simulation; Dassault Systemes: Vélizy-Villacoublay, France, 2014.
35. Rojíček, J.; Čermák, M.; Halama, R.; Paška, Z.; Vaško, M. Material Model Identification from Set of Experiments and Validation by DIC. *Math. Comput. Simul.* **2021**, *189*, 339–367. https://doi.org/10.1016/j.matcom.2021.04.007.
36. *ASME B36.10M*; Welded and Seamless Wrought Steel Pipe. American Society of Mechanical Engineers: New York, NY, USA, 2018.
37. *ASME B36.19M*; Stainless Steel Pipe. American Society of Mechanical Engineers: New York, NY, USA, 2018.
38. Yang, Y.; Zhu, H.; He, D.; Du, C.; Xu, L.; He, Y.; Zheng, Y.; Ye, Z. Contact Mechanical Behaviors of Radial Metal Seal for the Interval Control Valve in Intelligent Well: Modeling and Theoretical Study. *Energy Sci. Eng.* **2020**, *8*, 1337–1352. https://doi.org/10.1002/ese3.597.
39. Liu, Y.; Du, H.; Ren, X.; Li, B.; Qian, J.; Yan, F. A Leakage Rate Model for Metal-to-Metal Seals Based on the Fractal Theory of Porous Medium. *Aerospace* **2022**, *9*, 779. https://doi.org/10.3390/aerospace9120779.
40. Manikandan, H.; Chandra Bera, T. Modelling of Dimensional and Geometric Error Prediction in Turning of Thin-Walled Components. *Precis. Eng.* **2021**, *72*, 382–396. https://doi.org/10.1016/j.precisioneng.2021.05.013.
41. Abdalrahman, R.M.; Sure, S.A.H. The Influence of Cutting Edge Angles Included Angle and Nose Radius on Surface Finish of Aluminum Alloy 1050 in Turning. *Zanco J. Pure Appl. Sci.* **2020**, *32*, 31–38. https://doi.org/10.21271/zjpas.32.1.4.
42. Shao, Y.; Yin, Y.; Du, S.; Xia, T.; Xi, L. Leakage Monitoring in Static Sealing Interface Based on Three Dimensional Surface Topography Indicator. *J. Manuf. Sci. Eng.* **2018**, *140*, 101003. https://doi.org/10.1115/1.4040620.
43. *ISO 16610-41-2015*; Geometrical Product Specifications (GPS)-Filtration-Part 41: Morphological Profile Filters: Disk and Horizontal Line-Segment Filters. International Organization for Standardization: Geneva, Switzerland, 2015.
44. *ISO 16610-85-2013*; Geometrical Product Specifications (GPS)-Filtration-Part 85: Morphological Areal Filters: Segmentation. International Organization for Standardization: Geneva, Switzerland, 2015.
45. Chen, J.J.; Shih, Y.S. Study of the Helical Effect on the Thread Connection by Three Dimensional Finite Element Analysis. *Nucl. Eng. Des.* **1999**, *191*, 109–116. https://doi.org/10.1016/S0029-5493(99)00134-X.
46. Toupin, R.A. Saint-Venant's Principle. *Arch. Ration. Mech. Anal.* **1965**, *18*, 83–96. https://doi.org/10.1007/BF00282253.
47. Nitta, I.; Matsuzaki, Y. Experimental Study of the Performance of Static Seals Based on Measurements of Real Contact Area Using Thin Polycarbonate Films. *J. Tribol.* **2010**, *132*, 022202. https://doi.org/10.1115/1.4000838.
48. Georgescu, C.; Cristea, G.C.; Dima, C.; Deleanu, L. Evaluating Lubricating Capacity of Vegetal Oils Using Abbott-Firestone Curve. *IOP Conf. Ser. Mater. Sci. Eng.* **2017**, *174*, 012057. https://doi.org/10.1088/1757-899X/174/1/012057.
49. Prat, M.; Plouraboué, F.; Letalleur, N. Averaged Reynolds Equation for Flows between Rough Surfaces in Sliding Motion. *Transp. Porous Media* **2002**, *48*, 291–313. https://doi.org/10.1023/A:1015772525610.

50. *ASME B16.104*; Control Valve Seat Leakage. American Society of Mechanical Engineers: New York, NY, USA, 1998.
51. *ISO 21329:2004*; Petroleum And Natural Gas Industries-Pipeline Transportation Systems-Test Procedures for Mechanical Connectors. International Organization for Standardization: Geneva, Switzerland, 2004.